Journal of Materials Chemistry A

Accepted Manuscript

ROYAL SOCIETY OF CHEMISTRY

www.rsc.org/materialsA

Journal Name

RSCPublishing

ARTICLE

Hierarchical porous CNTs@NCS@MnO_2 composites: rational design and high asymmetric supercapacitor performance

Cite this: DOI: 10.1039/x0xx00000x

Received 00th January 2012,
Accepted 00th January 2012

DOI: 10.1039/x0xx00000x

www.rsc.org/

Lei Li,[a] Rumin Li,[a] Shili Gai,[a] Peng Gao,*[a] Fei He,[a] Milin Zhang,[a] Yujin Chen*[b] and Piaoping Yang*[a]

In this contribution, we present a novel and rational strategy for preparing hierarchical porous CNTs@NCS@MnO_2 core-shell composite *via* a facile *in situ* chemical polymerization coating method, followed by a hydrothermal process. The intermediate nitrogen-doped carbon shell (NCS) with mesoporous structure and favorable chemical durability is obtained by utilizing resorcinol-formaldehyde resin as carbon source and L-cysteine as nitrogen source, respectively. Benefiting from unique structure and considerable combination, the composites possess high comprehensive electrochemical performance: high specific capacitance (312.5 F/g at a current density of 1 A/g), good rate capability (76.8 % retention with charge-discharge rate increasing from 1 A/g to 10 A/g), superior reversibility and cycling stability (92.7% capacitance retention after 4000 cycles at 8 A/g). In order to increase the energy density and voltage window, an asymmetric supercapacitor (ASC) was assembled using CNTs@NCS@MnO_2 and activated carbon (AC) as the positive and negative electrodes, respectively. The as-fabricated asymmetric supercapacitor achieved a high specific capacitance with a stable operational voltage of 1.8 V and a maximum energy density of 27.3 Wh/kg. Such a synthetic route to prepare the capacitor materials can thoroughly motivate the synergistic effect between electrical double layer capacitors and pseudocapacitors for obtaining high comprehensive performance electrode in energy storage fields.

1. Introduction

Supercapacitors, possessing a range of favorable characteristics such as high power density, fast delivery rate and long cycle life, are emerging as one of the most promising energy storage to meet the tremendous increase in resource consumption in modern society.[1–5] Typically, supercapacitors can be classified into two major types depending on the charge-discharge mechanism: electrical double layer capacitors (EDLCs), whose charges are adsorbed electrostatically on the electrode/electrolyte accessible surface, are typically based on carbon materials; pseudocapacitors, such as conducting polymers and transition metal oxides, stores energy by utilizing fast and reversible faradaic reaction at the electrode interface.[6–8] Today, with the large proliferation of consumer electronics, advanced supercapacitors with higher energy density and operating voltage are urgently required for practical applications.[9–12] Among the recent energy storage technologies, developing and fabricating asymmetric supercapacitors, which can integrate appropriate electrode materials in complementary windows to increase the cell voltage, is an effective approach to meet the current demands.[13–17]

As one of the most attractive pseudocapacitive materials, MnO_2 has been extensively studied due to its significant superiorities such as reasonable cost, low toxicity and high theoretical specific capacitance (1370 F/g).[18–22] However, its poor electrical conductivity cannot support fast electron transport towards high rate capability, thus limiting the wide application. In order to improve the performance of MnO_2 electrode, two major strategies have been proposed to enhance its conductivity and capacitance. The first one is to synthesize nanostructured MnO_2 electrode with desirable architecture and high surface area.[23,24] The second method is to hybridize MnO_2 with conductive carbon-based materials.[25–28] In general, this kind of MnO_2/conductor composites exhibit better electrochemical performance compared to the pristine MnO_2 material owning to the positive effect of carbon-based materials, which can efficiently minimize the equivalent series resistance and further improve the power density of the composites.[21,29–31] With regard to carbon material, CNTs, with inspired features of excellent electrical conductivity, high mechanical strength and chemical stability, are often selected as a suitable substrate for MnO_2 deposition.[32–35] In addition, it is feasible and cheap to obtain hybrid materials by combining MnO_2 and CNTs based on the redox reaction: $4KMnO_4 + 3C + H_2O = 4MnO_2 + 2KHCO_3 + K_2CO_3$.[36–38] By this procedure, MnO_2 nanostructures can be well incorporated into carbon matrix, which can remarkably enhance its electrical conductivity.[39–41]

However, the limited accessible surface and micro-size pores of CNTs restrict the direct usage and the maximum mass loading of MnO_2 in a given area.[42,43] Moreover, it is difficult to prepare a highly conductive CNTs network due to the presence of a pseudo material layer between CNTs.[44,45] To solve this problem, a facile combination of CNTs and porous carbon has been presented to develop thick free-standing and mechanically/chemically stable conductive networks for MnO_2 deposition. In addition, it has been revealed that electrical properties of carbon-based supercapacitors could be improved through internal or surface doping of heteroatoms (such as N or S), resulting in enhanced specific capacitance. This it because carbon-based materials are beneficial due to their high surface-to-volume ratios and reduced transport lengths for both mass and charge transport in the field of electrochemical energy storage.[46–48]

Herein, with the aim of designing and assembling highly-efficient asymmetric supercapacitors (based on MnO_2 and CNTs), we developed a new and facile process to synthesize porous hierarchical CNTs@NCS@MnO_2 composites, which can make full use of the electrical conductivity of the CNTs and also motivate a synergistic effect from a combination of NCS and MnO_2 pseudo materials with tailored structure. The thick NCS shells, allowing highly areal density loading of MnO_2, were obtained by a simple and low-cost in situ chemical polymerization coating method, utilizing resorcinol-formaldehyde resin and L-cysteine as carbon and nitrogen source, respectively. With the aid of redox reaction between $KMnO_4$ and carbon, MnO_2 was coated uniformly with ultra-thin nanopetals under hydrothermal conditions. This unique double-core-shell structure can provide high microporosity and good electrical conductivity and create a short diffusion path, which is responsible for fast charge and discharge process and long life time. Furthermore, we also developed a novel ASC device based on CNTs/NCSs/MnO_2 as positive electrode and AC as the negative electrode in a Na_2SO_4 aqueous electrolyte. The electrochemical performance of this as-prepared ASC device has been systematically tested to confirm the practical applications in the fields of energy storage and conversion systems.

2. Experimental Section

2.1. Synthesis of the samples

Synthesis of CNTs@NCS composites. In a typical procedure, 0.1 g of CNTs were homogenously dispersed into 80 mL deionized water with the help of sonication for 6 h, followed by the addition of 0.25 g of L-cysteine, 0.553 g of resorcinol and 0.25 mL ammonia. After stirring at 40 °C for 0.5 h, 0.6 mL of formaldehyde was added slowly into the suspension and maintained for another 6 h. The black product was then collected, purified and dried overnight. The CNTs@NCS nanotubes were obtained by the carbonization under high pure nitrogen atmosphere at 650 °C for 3 h.

Synthesis of CNTs@NCS@MnO_2 composites. The uniform growing of MnO_2 nanosheets on the surface of NCS was conducted by dispersing certain amount of the CNTs@NCS into a Teflon-lined stainless autoclave containing a 0.01 M $KMnO_4$ solution, which was subsequently maintained at 160 °C for 1 h. After cooling to room temperature, the precipitate was collected by centrifugation, washed with deionized water, and dried at 60 °C to obtain the final CNTs@NCS@MnO_2 composites. For comparison, CNTs@MnO_2 composite was prepared by directly putting certain amount of CNTs into $KMnO_4$ solution under the same condition.

Electrode preparation and electrochemical measurement. In single-electrode tests, a three-electrode system was used to measure electrochemical performance of CNTs@NCS@MnO_2 composites, where the CNTs@NCS@MnO_2 electrode served as the working electrode, while a Pt wire and an Ag/AgCl electrode were used as the counter and a reference electrode, respectively. The working electrode was prepared by mixing CNTs@NCS@MnO_2 with acetylene black and polyvinylidene fluoride (5 wt.% in N-methyl-2-pyrrolidone solvent) with a weight ratio of 8:1:1. After thoroughly mixing, the slurry was pressed into thin Ni foam by a rolling method and then dried at 60 °C in a vacuum for 12 h. For the construction of an asymmetric supercapacitor device, CNTs@NCS@MnO_2 composites and activated carbon (AC) were respectively used as positive electrode and negative electrode (the preparation of the AC negative electrode was similar to that of CNTs@NCS@MnO_2 electrode), and a porous polymer membrane separator was employed as the supercapacitor separator. In order to obtain the mass balance, the mass ratio between the AC and CNTs@NCS@MnO_2 needs to follow: $m_+/m_- = C_- \cdot V_- / C_+ \cdot V_+$. According to the capacitance values (164 F/g for AC and 280 F/g for CNTs@NCS@MnO_2) calculated from the CV curves (Fig. S3) and the potential windows found for AC and CNTs@NCS@MnO_2, the mass ration should be 1.8, which can make full use of positive material. All the tests were carried out at room temperature with a 1 M Na_2SO_4 aqueous solution as the electrolyte. The specific capacitance values of the electrode were calculated from galvanostatic charge-discharge curves according to the following equation: $C = I\Delta t/m\Delta V$, where I is the response current density, Δt is the discharge time, m is the mass of the active materials on single electrode and total mass of the active materials on both the positive and negative electrode, ΔV is the potential range during the charge-discharge measurement. The energy density and power density of the asymmetric supercapacitor were calculated by following equations: $E = C_m\Delta V^2/2$, $P = E/\Delta t$, where C_m is the specific capacitance of the asymmetric supercapacitor, ΔV is the maximum voltage applied during the charge-discharge measurement, and Δt is the discharge time.

2.2. Characterization

Powder X-ray diffraction (XRD) measurements were performed on a Rigaku D/max TTR-III diffractometer at a scanning rate of 15° per min in the 2θ range from 10° to 80°, with graphite monochromatized Cu Kα radiation (λ = 0.15405 nm). Images were obtained digitally on scanning electron microscope (SEM, JSM-6480A), transmission electron microscopy (TEM, FEI Tecnai G^2 S-Twin) and high-resolution transmission electron microscopy (HRTEM). The X-ray photoelectron spectra (XPS) were recording on a VG ESCALAB MK II electron energy spectrometer using Mg KR (1253.6 eV) as the X-ray excitation source. N_2 adsorption/desorption isotherms were obtained on a Micromeritics ASAP Tristar II 3020 apparatus. Pore size distribution was calculated by the Barrete-Jonere-Halenda (BJH) method. The electrochemical properties was carried out by a CHI 666D electrochemical workstation. All of the measurements were performed at room temperature.

3. Results and discussion

3.1. Phase, structure, composition and morphology

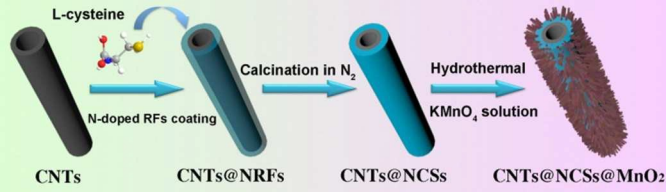

Scheme 1 Schematic illustration for the preparation of CNTs@NCS@MnO_2 composite.

The synthetic strategy of CNTs@NCS@MnO_2 nanohybrids is illustrated in Scheme 1. First, a thick layer of resins is uniformly coated on the surface of CNTs by *in situ* chemical polymerization of resorcinol-formaldehyde. In this process, the self-assembly of L-cysteine and RF, which were served as nitrogen and carbon source, can proceed in solution at 40°C. Afterwards, the carbonization from CNTs@NRF to CNTs@NCS was operated by annealing treatment in flowing N_2. To this end, the CNTs@NCS was immersed into $KMnO_4$ solution with a temperature of 160°C under hydrothermal conditions for the uniform growth of MnO_2 nanosheets, resulting in the ternary CNTs@NCS@MnO_2 composites with increased hierarchy. Due to consumption of the carbon source in the redox reaction between NCS and $KMnO_4$, an obvious cavity appears between the CNTs core and NCS@MnO_2 layer.

To understand the evolution process and identify the crystal structure of the samples, XRD patterns of the CNTs@NCS, CNTs@NCS@MnO_2 composite are shown in Fig. 1. It can be seen that the CNTs@NCS composite exhibits a sharp peak at around 26° and broad weak peak at 44°, which can be assigned to the (002) and (101) planes of graphite carbon.[49,50] For the CNTs@NCS@MnO_2 sample, obvious three peaks at about 13°, 38° and 68° can be indexed to the monoclinic structure of birnessite-type MnO_2 (JCPDS 42-1317, δ-MnO_2).[51,52] Notably, the intensity of the characteristic peak for graphic carbon at 26° become weak and the peak at 44° has disappeared simultaneously, which demonstrate that the MnO_2 nanosheets are uniformly grown on the surface of the NCS, resulting in the overwhelming of the signal of the graphite carbon.

The morphology and structure of CNTs@NCS composite were characterized by SEM and TEM images. As shown in Fig. 2A, CNT@NCS well preserves the one dimensional tubular

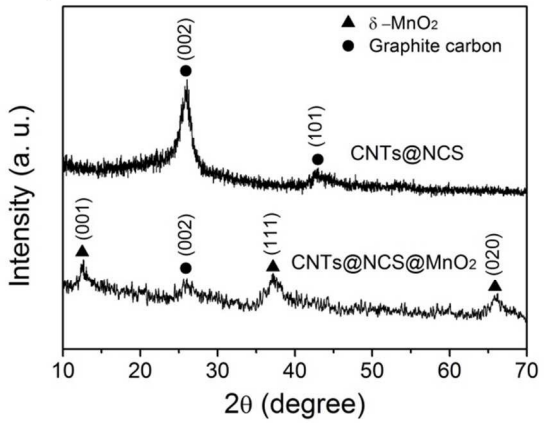

Fig. 1 XRD patterns of CNTs@NCS and CNTs@NCS@MnO_2 composite.

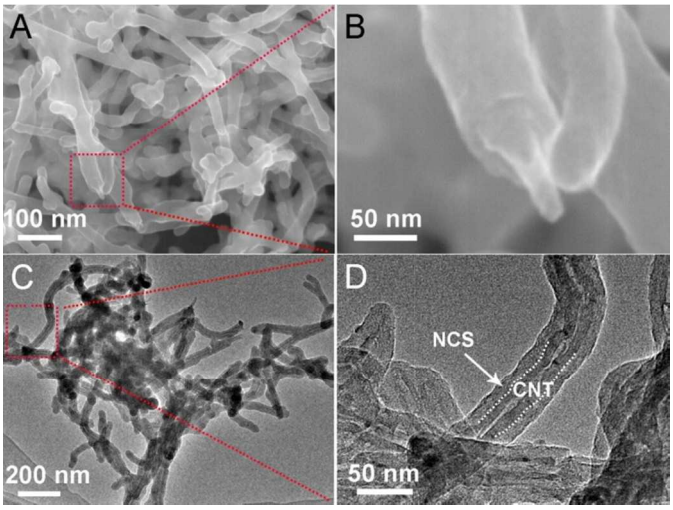

Fig. 2 SEM (A, B) and TEM (C, D) images of CNT@NCS composite.

structure of the CNTs and the average outer diameter has increased from 25 nm (pure CNTs) to 55 nm. The surface of CNTs is wrapped by NCS while protruding nanotubes ends are frequently exposed, clearly showing the core-shell structure (Fig. 2B). TEM images of the CNTs@NCS reveal that there is a uniform layer about 15 nm coated on the surface of the CNTs (Fig. 2C and D), indicating the strong shape and structure-directing role of the CNTs during the formation process. Due to the close integration between CNTs and NCS, the outer shell can be qualified to be an intermediate layer for anchoring MnO_2, which can prevent the detaching of the MnO_2 nanosheets from the smooth CNTs surface.

The SEM image of CNTs@NCS@MnO_2 composite is displayed in Fig. 3A. Clearly, the whole surface of the CNTs@NCS is almost covered by the nanoflakes of MnO_2, which provide interstitial space in the composites. The TEM image (Fig. 3B) shows that the outer layer of obtained CNTs@NCS@MnO_2 material is gradually substituted by MnO_2 during the redox reaction, manifesting that the NCS shell is applied as both reducing agents and substrates for MnO_2 growth. Closer observation (Fig. 3C) demonstrates that the cross-linked abundant, randomly assembled MnO_2 nanosheets grow upon the sidewalls of the middle NCS shell uniformly, and the interfacial profiles between the nanosheets and the tube can be well identified. It is worth noting that even after a long sonication time during preparation of the TEM specimen, MnO_2 nanosheets remain attached to the surface of the NCS shell and are not peeled off, implying that a strong interaction between MnO_2 and CNTs@NCS. Clear lattice fringes of the CNTs@NCS@MnO_2 composites are observed in the HRTEM image (Fig. 3D) and measured to be 0.7 nm, which can be assigned to (001) plane of the monoclinic δ-MnO_2.[53]

In Fig. 3E, a typical CNTs@NCS@MnO_2 nanotube is shown in high-angle annular dark field (HAADF) scanning transmission electron microscopy (STEM) image, confirming that MnO_2 nanosheets are evenly dispersed throughout the CNTs@NCS matrix. As shown in Fig. 3F, EDS line scanning (indicated by a line in Fig. 3E) of C, Mn and N across the nanotube can better illustrate that configuration: the profile of C shows a broad peak, which was mainly located at the center of the profile, while the profiles of Mn and N show higher intensity on both sides. The line clearly indicates the core-shell structure of the composite. The elemental composition of the CNTs@NCS@MnO_2 sample was analyzed using scanning

transmission electron microscopy energy-dispersive X-ray spectroscopy (STEM-EDS), which show the presence of C, Mn, N and O. From the mapping result, we can clearly distinguish the uniformly distributed MnO_2 and core-shell structure of the composite. The unique structure can not only provide more electrochemically active sites of MnO_2 to be assessed by electrolyte, but increase the effective liquid-solid interfacial area, promoting the surface redox reaction and EDLC formation. The nitrogen content detected can be ascribed to the successful doping of N element into carbon matrix.

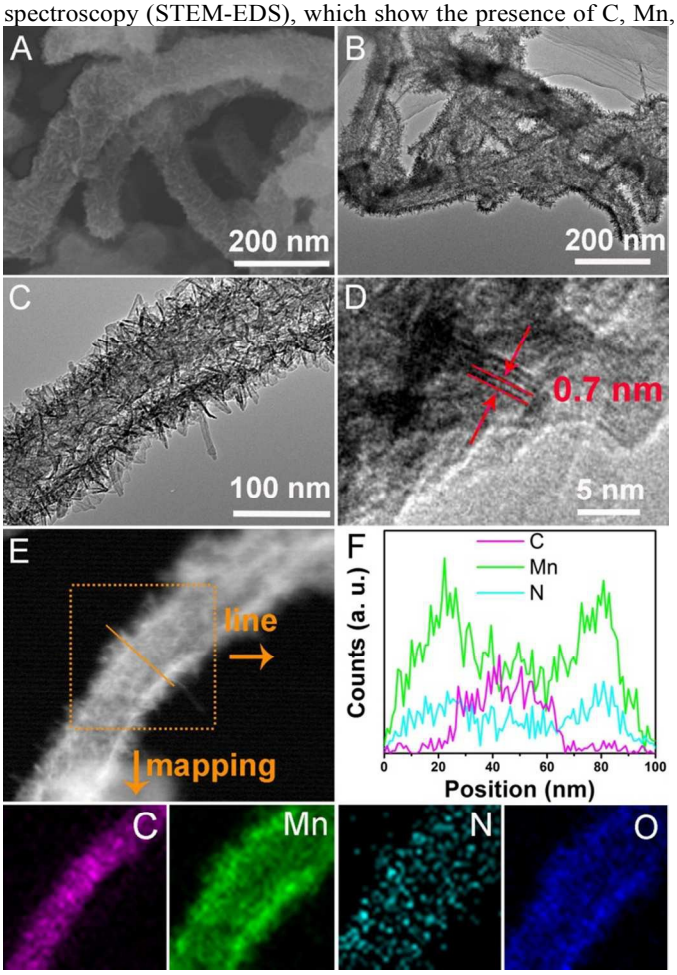

Fig. 3 SEM image (A), low- (B) and high-magnified (C) TEM images, HRTEM image (D), HAADF-STEM image (E) and elemental mapping images (G) of CNTs@NCS@MnO_2 composite. Panel F is the compositional line profile across the CNTs@NCS@MnO_2.

XPS analysis is employed in order to provide further evidence for the structural information of the CNTs@NCS@MnO_2 hybrid (Fig. 4A). reveals the existence of C, Mn, N and O, which is agreement with the EDS analysis. The high-resolution of C 1s spectrum (Fig. 4B) displays a dominant peak at 284.6 eV, accompanied with a shoulder peak at 285.7 eV and a minor foot peak at 287.8 eV, which are attributed to C=C, C-O and C-N groups, respectively. Thus, it can be concluded that the amorphous carbon originating from RFs is completely formed during the calcination process and nitrogen from L-cysteine was successfully introduced into carbon lattice. Previous reports demonstrate that the presence of nitrogen element in carbon-based materials can enhance the wettability of the carbon skeleton by the electrolyte and thus improve the mass-transfer efficiency.[46,48] The XPS pattern of N 1s is shown in Fig. 4C, where the three component peaks are assigned to graphitic N (401.3 eV), pyrrolic N (399.5 eV) and pyridinic N (398.6 eV).[36] According to the theoretical investigations, graphitic N can significantly increase the conductivity of carbon materials, while pyrrolic N and pyridinic N can crease numerous extrinsic defects and active sites, which

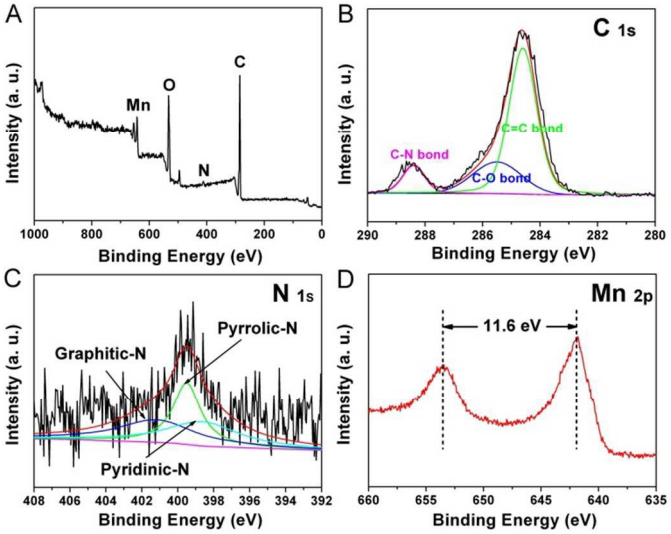

Fig. 4 XPS spectra of CNTs@NCS@MnO_2 composite: survey spectrum (A), C 1s (B), N 1s (C) and Mn 2p (D).

are beneficial for the fast diffusion of transporting ions and thus give rise to pseudocapacitance.[46,47] The Mn 2p spectrum in Fig. 4D shows the Mn $2p_{3/2}$ and Mn $2p_{1/2}$ binding energies are centered at 642.1 eV and 653.7 eV, respectively. The spin-energy separation between these two peaks is 11.6 eV, which is well consistent with the typical values of Mn (IV).[54,55]

Specific surface area and pore size are the two important parameters for the performance of a supercapacitor.[56,57] The N_2 adsorption-desorption isotherms and the corresponding pore size (inset) of CNTs@NCS@MnO_2 are shown in Fig. 5. The isotherm can be classified as type IV according to the profile of a hysteresis loop in relative pressure (P/P_0) range of 0.5–1.0, revealing that the CNTs@NCS@MnO_2 composite owns a typical mesoporous structure. The specific surface area and average pore size are calculated to be 180 m^2/g and 4.21 nm, respectively. The high surface area and moderate pore size (2–5 nm) of CNTs@NCS@MnO_2 enable the possibility of efficient transport of the electrons and ions in the electrode, hence leading to enhanced electrochemical property.

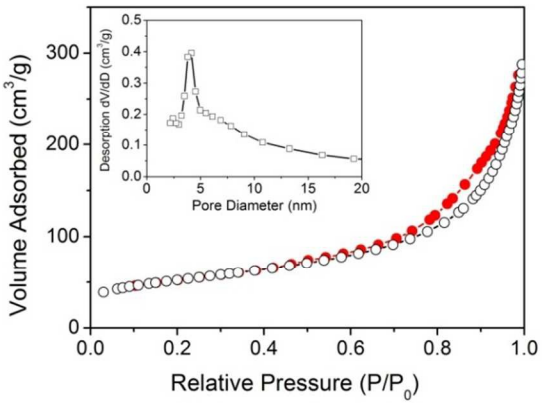

Fig. 5 N_2 adsorption/desorption isotherm and the corresponding pore size distribution (inset) of the CNTs@NCS@MnO_2 composite.

3.2. Electrochemical properties

Cyclic voltammetry (CV) was conducted to study the electrochemical performance of the as-prepared composite in a three-electrode cell in 1 M Na_2SO_4 electrolytes using Ag/AgCl electrode as reference electrode and a Pt as counter electrode. Fig. 6A compares the CV curves of CNT, CNTs@NCS, CNT@MnO_2 and CNTs@NCS@MnO_2 electrodes collected from 0 to 1.0 V at a the same scan rate of 30 mV/s. (the CV curves of CNTs@NCS and CNTs@MnO_2 are provided in Fig. S1 in electronic supporting information). Significantly, theCNTs@NCS@MnO_2 electrode exhibits substantially higher capacitive current density than those of CNTs@NCS and CNTs@MnO_2, suggesting the superior electrochemical performance and demonstrating the conductive NCS is good support for depositing MnO_2 nanosheets. Moreover, it can be seen that the CNTs@NCS@MnO_2 shows a relatively rectangular and symmetric shapes, indicating the ideal supercapacitor behavior.[58,59] In Fig. 6B, the CV curves of the CNTs@NCS@MnO_2 composite are quasi-rectangular shaped up to a 100 mV/s scan rate, and the distortion of them is inconspicuous, implying that the system of the electrodes has low contact resistance and good rate performance.

In order to evaluate the power application of as-prepared CNTs@NCS@MnO_2, charge-discharge test was performed at various current densities from 0 to 1 V as shown in Fig. 6C. All the galvanostatic charge-discharge curves are nearly liner and the discharge curves are almost symmetrical to the corresponding charge curves with negligible IR drop, indicating a low internal resistance, excellent reversibility and high Coulombic efficiency. The correlation between the specific capacitance and current densities from 1 to 10 A/g for different electrodes is presented in Fig. 6D. The specific capacitance of each sample is calculated based on galvanostatic discharge time (the galvanostatic charge-discharge curves of CNTs, CNTs@NCS and CNTs@$MnO_2$are provided in Fig. S1 and Fig. S2 in electronic supporting information). Obviously, the CNTs@NCS@MnO_2 possesses the highest specific capacitance among all electrodes at the same current densities, which is consistent with the CV tests. Furthermore, the specific capacitance of CNTs@NCS@MnO_2 is as high as 312.5 F/g at a current density of 1 A/g and maintains at 240.2 F/g with a retention ratio of 76.8 % at 10 A/g, suggesting that the composite has a good rate capability, which is indispensable for the practical applications. The enhancement in specific capacitance and rate capability can be ascribed to the interconnected porous NCS. On one hand, the unique structureof NCS can provide unimpeded diffusion channel and facile accessibility of active sites for electrolyte ions. On the other hand, the NCS with large surface area can act as substrate and guarantee the fine dispersion of MnO_2 nanosheet, leading to the positive synergistic effect between the conductive carbon material and pseudocapacitive MnO_2.

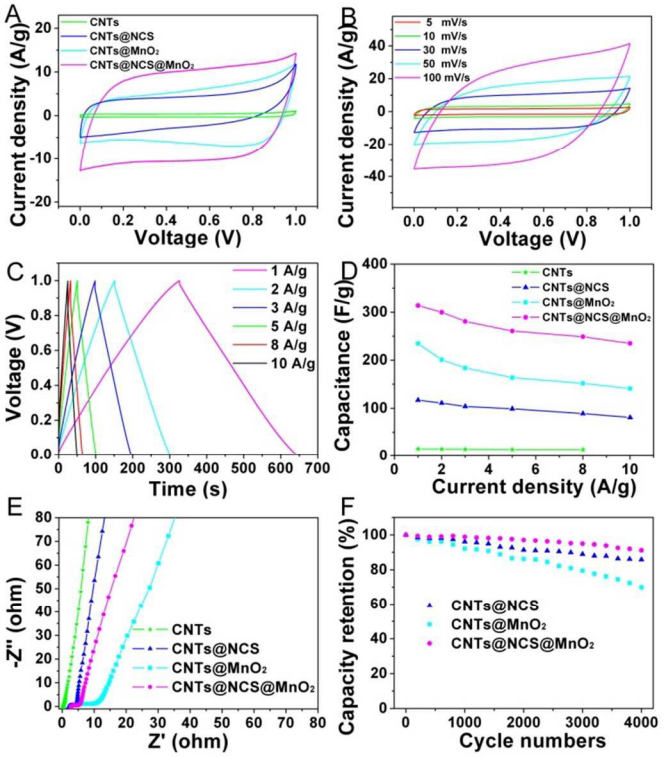

Fig. 6 Cyclic voltammograms at 30 mV/s for pure CNTs, CNTs@NCS, CNTs@MnO_2 and CNTs@NCS@MnO_2 (A). CV curves at scan rates from 5~100 mV/s (B) and galvanostatic charge-discharge curves measured at various discharge current (C) of CNTs@NCS@MnO_2 composite. Current density dependence of the specific capacitance (D), Nyquist plots of the EIS (E), and cycling performance (F) for CNTs, CNTs@NCS, CNTs@MnO_2 and CNTs@NCS@MnO_2.

Electrochemical impedance spectroscopy (EIS) was carried out to further understand the kinetics of the electrode process, that is, the interaction between electrode and electrolyte. As shown in Fig. 6E, each Nyquist plot displays a semicircle in high-frequency and a straight line in the low-frequency region, which signify light electrochemical polarization and good capacitive property.[39,60] The intercept on the real axis reveals the equivalent series resistance (Rs), and the diameter of the semicircle corresponds to the charge transfer resistance (Rct) at the electrode/electrolyte interface. Except for the pure CNTs, the Rs of the hybrid CNTs electrodes are approximate. However, the CNTs@NCS@MnO_2 electrode exhibits smaller Rct than CNTs@MnO_2 composite in high-frequency region, which demonstrates that unique structure of the CNTs@NCS@MnO_2 can facilitate the penetration of the electrolyte into the electrode and greatly increases the interface between the electrode and electrolyte. Also, it can be seen that the CNTs@NCS@MnO_2 has a vertical straight line than that of CNTs@MnO_2, suggesting that the CNTs@NCS@MnO_2 has lower diffusive resistance to electrolyte and faster ion transport speed than the CNTs@MnO_2. The EIS result confirms that the conductivity of CNTs@NCS@MnO_2 can be significantly improved by the introduction of NCS, which will favor rate capability for high power performance and enhance the utilization of the electrode.

Cycle stability is an important requirement in practical applications, which was investigated with a charge-discharge current density of 8 A/g for 4000 repetitive cycles, as shown in Fig. 6F. The CNTs@NCS@MnO_2 electrode exhibits a capacitive retention of 92.70 %, which is much better than that of the CNTs@NCS (87%) and CNTs@MnO_2 (65%), implying that the CNTs@NCS@MnO_2 composite possesses ideal long-term electrochemical stability even at high current density. Such an excellent stability coupled with the low resistance and unique porous structure ensures the CNTs@NCS@MnO_2 material to be a qualified electrode candidate for energy storage applications.

To further evaluate the CNTs@NCS@MnO_2 electrode for practical applications, an asymmetric supercapacitor device was fabricated by employing CNTs@NCS@MnO_2 and AC

composites as positive and negative electrodes, respectively, in 1 M Na_2SO_4 aqueous solution, as shown in Fig. 7A. Taking

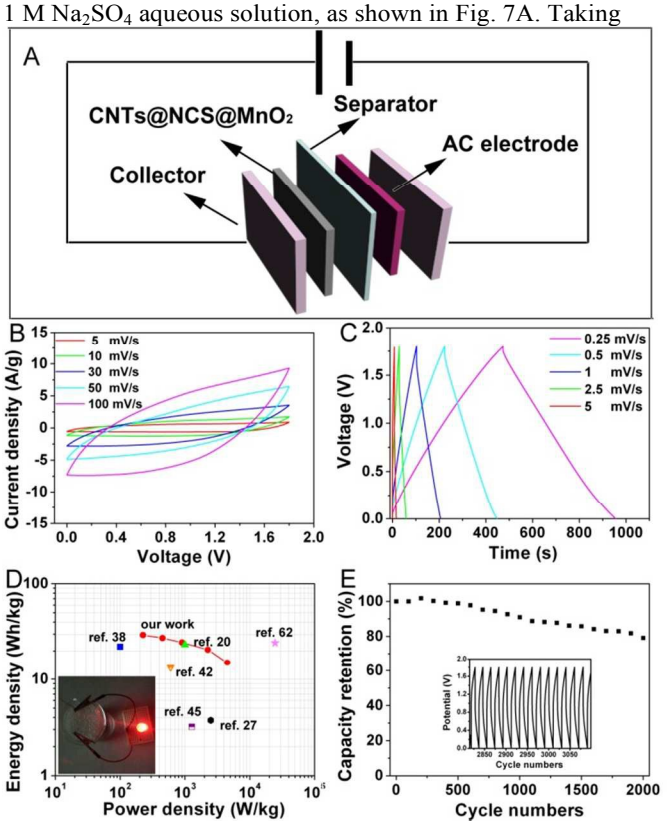

Fig. 7 Schematic structure of as-made asymmetric supercapacitor consisting of CNTs@NCS@MnO_2 and AC electrodes, a separator, and two current collectors (A), CV curves of the as-assembled ASC at different scan rates (B), Galvanostatic charge/discharge curves of ASC device collected at different current densities (C), Ragone plot of the ASC device (D), inset is the photo image of four red LEDs powered by the ASC device. Cycling performance of ASC device at 5 A/g, inset is the charge/discharge curve at 5 A/g (E).

advantages of different potential windows of the two materials, the ASC device promises a wide operating voltage and thus provides increased energy densities. As shown in Fig. 7B, the CV curves of the ASC have been measured between 0 and 1.8 V at scan rates range from 5 to 100 mV/s, which exhibit good symmetrical and approximately rectangular without obvious redox peaks. This result suggests that both the surface and electrosorption of ions and the redox reaction of anions are well matched in this device, which can be ascribed to fast electrosorption of Na^+ cations and the subsequent quick reversible faradaic process proceeding from Na^+ cations and MnO_2.

Galvanostatic charge-discharge curves of the ASC at various current densities in a voltage window from 0 to 1.8 V are given in Fig. 7C. Good linear profiles of the curves, the charge curves are symmetrical to their corresponding discharge counterparts, can further confirm the perfect electrochemical behavior of the as-fabricated ASC in the whole potential range. On the basis of galvanostatic charge-discharge curves, Ragone plot of the device depicting the relation between energy density and power density is obtained, which is depicted in Fig. 7D. The maximum energy density and power density of 27.3 Wh/kg and 4500 W/kg can be achieved at an operating voltage of 1.8 V, which can easily light up the light–emitting diodes (LEDs). Significantly, the energy density in our work is higher than many previously reported devices.[20,27,38,42,45,61,62]

To test the long-term cycling performance of this ASC, consecutive charge-discharge cycles were performed at a considerable current density of 5 A/g. As shown in Fig. 7E, 78.8 % of the specific capacitance is maintained after repetitive 2000 cycles and the charge-discharge curves (inset in Fig. 7E) remain linear and symmetrical shape, demonstrating excellent cycling stability and high Coulombic efficiency.

Conclusions

In summary, we have demonstrated the design and synthesis of a new type of high-performance capacitor material CNTs@NCS@MnO_2 composite, and explored its practical application as positive electrode in asymmetric supercapacitor. Owing to the synergy effect from a combination of NCS and MnO_2 with tailored structure, the CNTs@NCS@MnO_2 electrode exhibits high comprehensive electrochemical performance: high specific capacitances, good rate capability, excellent reversibility and superior cycling stability. Moreover, a two-electrode asymmetric supercapacitor based on CNTs@NCS@MnO_2 and AC was fabricated and it delivers a high specific energy density and a good rate capability, as well as an excellent cycling stability. Therefore, we envision this ternary hybrid to be a promising electrode material for practical applications in the field of energy storage and conversion systems.

Acknowledgements

This work was supported by financial supports from National Natural Science Foundation of China (NSFC 21271053, 21401032, 51472058), NCET in University (NCET-12-0622), Natural Science Foundation of Heilongjiang Province (B201403), Harbin Sci.-Tech. Innovation Foundation (2014RFQXJ019) and Fundamental Research Funds for the Central Universities of China.

Notes and references

a Key Laboratory of Superlight Materials and Surface Technology, Ministry of Education, College of Material Science and Chemical Engineering, Harbin Engineering University, Harbin 150001, P. R. China. E-mail: yangpiaoping@hrbeu.edu.cn; gaopeng@hrbeu.edu.cn
b College of Science, Harbin Engineering University, Harbin 150001, P. R. E-mail: chenyujin@hrbeu.edu.cn

† Electronic Supplementary Information (ESI) available: Charge-discharge curves of CNTs@NCS and CNTs@MnO_2 measured at various discharge current. See DOI: 10.1039/b000000x/

1 L. L. Zhang and X. S. Zhao, *Chem. Soc. Rev.*, 2009, **38**, 2520-2531.
2 H. Wang, H. S. Casalongue, Y. Liang and H. Dai, *J. Amer. Chem. Soc.*, 2010, **132**, 7472-7477.
3 B. You, N. Li, H. Zhu, X. Zhu and J. Yang, *Chemsuschem*, 2013, **6**, 474-480.
4 D. N. Futaba, K. Hata, T. Yamada, T. Hiraoka, Y. Hayamizu, Y. Kakudate, O. Tanaike, H. Hatori, M. Yumura and S. Iijima, Nat. *Mater.*, 2006, **5**, 987-994.
5 L. Yu, L. Zhang, H. B. Wu and X. W. Lou, *Angew. Chem. Int. Ed.*, 2014, **53**, 3711-3714.
6 Y. Xu, M. G. Schwab, A. J. Strudwick, I. Hennig, X. Feng, Z. Wu and K. Muellen, *Adv.Energy.Mater.*, 2013, **3**, 1035-1040.
7 B. You, J. Jiang and S. Fan, *ACS applied materials & interfaces*, 2014, **6,** 15302-15308.

8 H. B. Wu, H. Pang and X. W. Lou, *Energ. Environ. Sci* , 2013, **6**, 3619-3626.
9 P. Yang, Y. Ding, Z. Lin, Z. Chen, Y. Li, P. Qiang, M. Ebrahimi, W. Mai, C. P. Wong and Z. L. Wang, *Nano Lett.*, 2014, **14**, 731-736.
10 L. Jiang and Z. Fan, *Nanoscale*, 2014, **6**, 1922-1945.
11 F. Beguin, V. Presser, A. Balducci and E. Frackowiak, *Adv. Mater.*, 2014, **26**, 2219-2251.
12 G. H. Yu, L. B. Hu, N. A. Liu, H. L. Wang, M. Vosgueritchian, Y. Yang, Y. Cui and Z. A. Bao, *Nano letters*, 2011, **11**, 4438-4442.
13 J. Zhang, J. Jiang, H. Li and X. S. Zhao, *Energ. Environ. Sci* , 2011, **4**, 4009-4015.
14 Q. Qu, P. Zhang, B. Wang, Y. Chen, S. Tian, Y. Wu and R. Holze, *J. Phys. Chem. C*, 2009, **113**, 14020-14027.
15 T. Brousse, P.-L. Taberna, O. Crosnier, R. Dugas, P. Guillemet, Y. Scudeller, Y. Zhou, F. Favier, D. Belanger and P. Simon, *J. Power Sources*, 2007, **173**, 633-641.
16 H. Chen, J. Jiang, Y. Zhao, L. Zhang, D. Guo and D. Xia, *J. Mater. Chem. A*, 2015, **3**, 428-437.
17 Q. Li, X. F. Lu, H. Xu, Y. X. Tong and G. R. Li, *ACS Appl. Mat. Interfaces*, 2014, **6**, 2726-2733.
18 Q. Chen, Y. Meng, C. Hu, Y. Zhao, H. Shao, N. Chen and L. Qu, *J. Power Sources*, 2014, **247**, 32-39.
19 Y. Huang, Y. Li, Z. Hu, G. Wei, J. Guo and J. Liu, *J. Mater. Chem. A*, 2013, **1**, 9809-9813.
20 H. Gao, F. Xiao, C. B. Ching and H. Duan, *ACS Appl. Mat. Interfaces*, 2012, **4**, 2801-2810.
21 S. Chen, J. W. Zhu, X. D. Wu, Q. F. Han and X. Wang, *ACS Nano*, **2010**, 4, 2822-2830.
22 P. Li, Y. Yang, E. Shi, Q. Shen, Y. Shang, S. Wu, J. Wei, K. Wang, H. Zhu, Q. Yuan, A. Cao and D. Wu, *ACS Appl. Mat. Interfaces* , 2014, **6**, 5228-5234.
23 T. Zhai, S. Xie, M. Yu, P. Fang, C. Liang, X. Lu and Y. Tong, *Nano Energy*, 2014, **8**, 255-263.
24 P. Yang, Y. Ding, Z. Lin, Z. Chen, Y. Li, P. Qiang, M. Ebrahimi, W. Mai, C. P. Wong and Z. L. Wang, *Nano Lett.*, 2014, **14**, 731-736.
25 M. Kim, Y. Hwang, K. Min and J. Kim, *Electrochim. Acta*, 2013, **113**, 322-331.
26 W. Tang, Y. Y. Hou, X. J. Wang, Y. Bai, Y. S. Zhu, H. Sun, Y. B. Yue, Y. P. Wu, K. Zhu and R. Holze, *J. Power Sources*, 2012, **197**, 330-333.
27 Y. M. He, W. J. Chen, X. D. Li, Z. X. Zhang, J. C. Fu, C. H. Zhao and E. Q. Xie, *ACS Nano*, 2013, **7**, 174-182.
28 K. Kai, Y. Kobayashi, Y. Yamada, K. Miyazaki, T. Abe, Y. Uchimoto and H. Kageyama, *J. Mater. Chem.*, 2012, **22**, 14691-14695.
29 J.-X. Feng, Q. Li, X.-F. Lu, Y.-X. Tong and G.-R. Li, *J. Mater. Chem. A*, 2014, **2**, 2985-2992.
30 M. Yan, F. Wang, C. Han, X. Ma, X. Xu, Q. An, L. Xu, C. Niu, Y. Zhao, X. Tian, P. Hu, H. Wu and L. Mai, *J. Amer. Chem. Soc.*, 2013, **135**, 18176-18182.
31 Y. Su and I. Zhitomirsky, *J. Power Sources*, 2014, **267**, 235-242.
32 Z. Dong, C. Zhou, H. Cheng, Y. Zhao, C. Hu, N. Chen, Z. Zhang, H. Luo and L. Qu, *Carbon*, 2013, **64**, 507-515.
33 S. Li, C. Zhao, K. Shu, C. Wang, Z. Guo, G. G. Wallace and H. Liu, *Carbon*, 2014, **79**, 554-562.
34 H. Jiang, C. Li, T. Sun and J. Ma, *Nanoscale*, 2012, **4**, 807-812.
35 J. Liu, M. Chen, L. Zhang, J. Jiang, J. Yan, Y. Huang, J. Lin, H. J. Fan and Z. X. Shen, *Nano Lett.*, 2014, **14**, 7180-7187.
36 D. Yu, K. Goh, Q. Zhang, L. Wei, H. Wang, W. Jiang and Y. Chen, *Adv. Mater.*, 2014, **26**, 6790-6797.
37 S. He, C. Hu, H. Hou and W. Chen, *J. Power Sources*, 2014, **246**, 754-761.
38 Z. Lei, J. Zhang and X. S. Zhao, *J. Mater. Chem.*, 2012, **22**, 153-160.
39 T. Zhai, F. Wang, M. Yu, S. Xie, C. Liang, C. Li, F. Xiao, R. Tang, Q. Wu, X. Lu and Y. Tong, *Nanoscale*, 2013, **5**, 6790-6796.
40 Y. Hou, Y. Cheng, T. Hobson and J. Liu, *Nano Lett.*, 2010, **10**, 2727-2733.
41 Y. Jin, H. Chen, M. Chen, N. Liu and Q. Li, *ACS Appl. Mat. Interfaces*, 2013, **5**, 3408-3416.
42 L. Li, Z. A. Hu, N. An, Y. Y. Yang, Z. M. Li and H. Y. Wu, *J. Phys. Chem. C*, 2014, **118**, 22865-22872.
43 M. Liu, W. W. Tjiu, J. Pan, C. Zhang, W. Gao and T. Liu, *Nanoscale*, 2014, **6**, 4233-4242.
44 G. Zhu, Z. He, J. Chen, J. Zhao, X. Feng, Y. Ma, Q. Fan, L. Wang and W. Huang, *Nanoscale*, 2014, **6**, 1079-1085.
45 Y. Cheng, S. Lu, H. Zhang, C. V. Varanasi and J. Liu, *Nano Lett.*, 2012, **12**, 4206-4211.
46 B. You, L. Wang, L. Yao and J. Yang, *Chem. Commun*. 2013, **49**, 5016-5018.
47 A. R. John and P. Arumugam, *J. Power Sources*, 2015, **277**, 387-392.
48 B. You, P. Yin and L. An, *Small*, 2014, **10**, 4352-4361.
49 H. Zheng, J. Wang, Y. Jia and C. a. Ma, *J. Power Sources*, 2012, **216**, 508-514.
50 H. B. Zhao, J. Yang, T. T. Lin, Q. F. Lu and G. Chen, *Chem. Eur. J.*, 2015, **21**, 682-690.
51 J. Zhu, W. Shi, N. Xiao, X. Rui, H. Tan, X. Lu, H. H. Hng, J. Ma and Q. Yan, *ACS Appl. Mat. Interfaces* , 2012, **4**, 2769-2774.
52 Y. Wang, S. F. Yu, C. Y. Sun, T. J. Zhu and H. Y. Yang, *J. Mater. Chem.*, 2012, **22**, 17584-17588.
53 Z. Li, Y. Mi, X. Liu, S. Liu, S. Yang and J. Wang, *J. Mater. Chem.*, 2011, **21**, 14706-4711.
54 L. Yuan, X.-H. Lu, X. Xiao, T. Zhai, J. Dai, F. Zhang, B. Hu, X. Wang, L. Gong, J. Chen, C. Hu, Y. Tong, J. Zhou and Z. L. Wang, *ACS Nano*, 2012, **6**, 656-661.
55 H. Jiang, J. Ma and C. Li, *Adv. Mater.*, 2012, **24**, 4197-4202.
56 H. Jiang, P. S. Lee and C. Li, *Energ. Environ. Sci* , 2013, **6**, 41-53.
57 Z.-S. Wu, G. Zhou, L.-C. Yin, W. Ren, F. Li and H.-M. Cheng, *Nano Energy*, 2012, **1**, 107-131.
58 Y. Tang, Y. Liu, W. Guo, T. Chen, H. Wang, S. Yu and F. Gao, *J. Phys. Chem. C*, 2014, **118**, 24866-24876.
59 X. Li and B. Wei, *Nano Energy*, 2012, **1**, 479-487.
60 W. Chen, R. B. Rakhi, L. Hu, X. Xie, Y. Cui and H. N. Alshareef, *Nano Lett.*, 2011, **11**, 5165-5172.
61 K. Xu, W. Li, Q. Liu, B. Li, X. Liu, L. An, Z. Chen, R. Zou and J. Hu, *J. Mater. Chem. A*, 2014, **2**, 4795-4802.
62 X. Zhao , L. L. Zhang , S. Murali , M. D. Stoller , Q. H. Zhang , Y. W. Zhu , R. S. Ruoff , *ACS Nano* 2012 , **6** , 5404-5412.

Hierarchical porous CNTs@NCS@MnO_2 composite was synthesized by a facile *in situ* chemical polymerization coating method, followed by a hydrothermal process, which exhibits high asymmetric performance.